Benchmark performance of low-cost Sb_2Se_3 photocathodes obtained by the fast-cooling strategy during close space sublimation for unassisted solar overall water splitting

Wooseok Yang[‡1], Jin Hyun Kim[‡2], Oliver S. Hutter[3], Laurie J. Phillips[3], Jeiwan Tan[1], Jaemin Park[1], Hyungsoo Lee[1], Jonathan D. Major[*3], Jae Sung Lee[*2], and Jooho Moon[*1]

[1] Department of Materials Science and Engineering, Yonsei University, 50 Yonsei-ro, Seodaemun-gu, Seoul, 03722, Republic of Korea
E–mail: jmoon@yonsei.ac.kr

[2] School of Energy and Chemical Engineering, Ulsan National Institute of Science and Technology, Ulsan, South Korea.
E-mail: jlee1234@unist.ac.kr

[3] Stephenson Institute for Renewable Energy, Physics Department, University of Liverpool, Liverpool L69 7XF, UK
E-mail: Jon.Major@liverpool.ac.uk

KEYWORDS: unassisted water splitting, Sb_2Se_3, tandem cell, close space sublimation, 1D ribbons

‡These authors contributed equally

ABSTRACT

Determining earth-abundant semiconductors exhibiting desirable properties for commercial photoelectrochemical water splitting remains a challenge. Herein, we report a Sb_2Se_3 semiconductor that satisfies most requirements for an ideal high-performance photoelectrode, including a small band gap and favourable cost, optoelectronic properties, processability, and photocorrosion stability. Strong anisotropy, a major issue for Sb_2Se_3, was resolved by suppressing growth kinetics via close space sublimation to obtain high-quality compact thin films with favourable crystallographic orientation. The Sb_2Se_3 photocathode exhibited a high photocurrent density of almost 30 mA cm^{-2} at 0 V against the reversible hydrogen electrode, the highest value so far. We demonstrated unassisted solar overall water splitting by combining the optimised Sb_2Se_3 photocathode with a $BiVO_4$ photoanode, achieving a solar-to-hydrogen efficiency of 1.5% with stability over 10 h under simulated 1 sun conditions employing a broad range of solar fluxes. Earth-abundant Sb_2Se_3 can thus be an attractive breakthrough material for commercial solar fuel production.

Molecular hydrogen production via photoelectrochemical (PEC) splitting of water is a promising solution toward a zero-carbon-based society. In order to produce sustainable H_2 for a scale commensurate with the global energy demand, high efficiency and low cost, both of which highly depend on the semiconductor materials used in the PEC system, should be achieved. As the solar-to-hydrogen (STH) efficiency of PEC devices using expensive photovoltaic-grade III-V semiconductors has approached the theoretical maximum[1], the research community is now recognising the importance of exploring low-cost materials exhibiting good optoelectronic properties[2]. With this consideration, nearly all recent critical evaluations[3-5] pertaining to artificial photosynthesis have urged the development of new light absorbers. According to theoretical calculations[6,7], two different light absorbers—having a band gap (E_g) of ~1.8 eV for the top electrodes and 1.0−1.3 eV for the bottom electrodes—are required for realising STH efficiencies of over 23% in the D4 (dual light absorber: four photons to one H_2) tandem cell. Further requirements for suitable semiconductors for PEC water splitting include a large light absorption coefficient (α), high mobility, easy processability without secondary phases, and stability to photocorrosion. In this regard, most emerging cost-competitive photoelectrode materials for PEC water splitting, such as TiO_2 (E_g ~ 3.2 eV)[8], Fe_2O_3 (E_g ~ 2.2 eV)[9], $BiVO_4$ (E_g ~ 2.4 eV)[10], and Cu_2O (E_g ~ 2.0 eV)[11], are deemed unsuitable for the bottom photoelectrode due to their large E_g. Although the E_g of $Cu_2ZnSn(S,Se)_4$ semiconductor, which is another earth-abundant material applicable for PEC water splitting, varies from 1.0 eV to 1.5 eV depending on the composition, the pure-phase compound suffers from severe difficulty of synthesis due to the narrow stoichiometric window[12]. It is worth mentioning that the secondary phase issue, i.e. the formation of undesirable detrimental phases during processing, could pose a major obstacle to large-scale commercialisation. In recent years, various low-cost semiconductors have emerged, such as Cu_2S (E_g ~ 1.5 eV)[13], $CuFeO_2$ (E_g ~ 1.5 eV)[14], $CuBi_2O_4$ (E_g ~ 1.7 eV)[15], $CuSbS_2$ (E_g ~ 1.5eV)[16], and SnS (E_g ~ 1.3 eV)[17].

However, none of them have satisfied all the requirements for an ideal semiconductor for PEC water splitting. Therefore, a breakthrough material for realising practical solar-to-hydrogen conversion is urgently required.[4]

Sb_2Se_3 offers many advantageous properties that make it a nearly ideal semiconductor material for PEC water splitting. First, it has a small E_g of 1.1−1.2 eV. In addition, it is a low-cost semiconductor (the cost of Sb is similar to that of Cu)[18] and exhibits attractive optoelectronic properties ($\alpha > 10^5$ cm^{-1} and high mobility of ~10 $cm^2 V^{-1}s^{-1}$)[19,20]. Moreover, the thermodynamic properties of the Sb-Se system allow only stable orthorhombic Sb_2Se_3 phases without any secondary phases[21], avoiding severe secondary phase issues commonly observed in other multivalent compound materials. It has also been reported that Sb_2Se_3 is intrinsically stable towards photocorrosion in strong acidic media unlike Cu_2O, which is vulnerable to photocorroson[22]. Owing to these merits, the photocurrent density of the Sb_2Se_3 photocathode has improved rapidly from the initially reported value of 2.5 mA cm^{-2} to 17.5 cm^{-2} at 0 V against the reversible hydrogen electrode (RHE) over the short period of its development[23-26]. However, it is still far below the theoretical maximum (about 40 mA cm^{-2}, assuming a 1.2 eV E_g and a 100% incident photon-to-current efficiency (IPCE)). In addition, it has been reported that the onset potential of Sb_2Se_3 photocathodes can be enhanced up to 0.47 V_{RHE} by inserting a CdS buffer layer between Sb_2Se_3 and TiO_2[27], but the photovoltage and fill factor should be further improved to realise unassisted water splitting.

this work, we have addressed important issues presented by the Sb_2Se_3 absorber arising from its strong anisotropic nature. As Sb_2Se_3 has a one-dimensional (1D) crystal structure, comprising strongly covalent Sb–Se bonds along the [001] direction and weak van der Waals forces among 1D $(Sb_4Se_6)_n$ ribbons along the [100] and [010] directions, it tends to grow with the morphology of 1D nanostructures, which makes synthesis of compact Sb_2Se_3

thin films difficult[28]. For example, a previous solution-based approach using a mixture of thioglycolic acid and ethanolamine yielded Sb_2Se_3 nanorod and nanowire arrays depending on the solvent ratio[24]. A different combination of 2-mercaptoethanol and ethylenediamine was also used to synthesise Sb_2Se_3 nanowire films[27]. In the case wherein a light-absorbing material has a low absorption coefficient and poor electrical properties (e.g. short carrier diffusion length), 1D nanostructuring could be an attractive strategy for enhancing the performance. However, in the previously reported Sb_2Se_3 photocathodes, probably owing to its good optoelectronic properties, planar-type Sb_2Se_3 exhibited better performance compared with that of its elongated 1D structured counterpart[24,27]. One possible reason is that the incomplete coverage of Sb_2Se_3 films, due to the complicated 1D morphology, can result in direct contact between the substrate and an n-type layer, which acts as a recombination centre. In addition, because the carrier transport in Sb_2Se_3 along the [001] direction is more efficient than that along the [010] and [100] directions owing to its anisotropic crystallographic nature[20], the p–n junction should be formed along the [001] direction to maximise the separation of the photo-generated charges. In the 1 D Sb_2Se_3 system, however, the p-n junction generally is formed along the [010] or [100] directions, resulting in inefficient charge separation, as schematically illustrated in Supplementary Fig. 1. Thus, compact film-type Sb_2Se_3 with favourable crystallographic orientation for efficient charge separation (i.e. vertically aligned $(Sb_4Se_6)_n$ nanoribbons) should be obtained to achieve high-performance Sb_2Se_3 photocathodes. However, as molecular inks for Sb_2Se_3 already contain 1D $[Sb_4Se_7]^{2-}$ chains in the solution[24,27], it is a daunting task to obtain compact thin Sb_2Se_3 films via solution processing.

Here, we report high-quality dense Sb_2Se_3 thin films obtained by the close space sublimation (CSS) method, which is known to be a low-cost, large-area, high-yield deposition technique for preparing light-absorbing semiconductors such as cadmium telluride[29] and $CH_3NH_3PbI_3$[30]. We implemented a fast cooling strategy as well as the two-step CSS method[31],

enabling pin-hole free and smooth Sb_2Se_3 thin films with well-oriented $(Sb_4Se_6)_n$ ribbons. The resulting Sb_2Se_3 thin film-based photocathodes revealed a highest photocurrent density close to 30 mA cm^{-2} at 0 V_{RHE} in an acidic electrolyte by harvesting a broad range of photons up to 1000 nm. Such extraordinary performance of the newly developed Sb_2Se_3 photocathode was utilised by unassisted overall water splitting PEC cells for the first time after judiciously optimising the photovoltage and electrolyte compatibility to the $BiVO_4$ photoanode. The D4 tandem cell of Sb_2Se_3–$BiVO_4$ in a neutral phosphate buffer successfully demonstrated an impressive STH efficiency of 1.5% with 10 h of stability. Realisation of the Sb_2Se_3-based tandem device, capable of harvesting a broad range of photons with the readily obtained earth-abundant semiconductor, allows us to envision practical solar hydrogen production via efficient and cost-competitive PEC water splitting.

Results and discussion

Fabrication of compact and well-oriented Sb_2Se_3 thin films

In order to avoid the formation of the thermodynamically favourable 1D structure as well as induce the metastable thin film morphology of Sb_2Se_3, we tried to kinetically suppress the rearrangement of $(Sb_4Se_6)_n$ nanoribbons by employing a two-step deposition where a low-temperature (340 °C) seed layer was deposited prior to the high-temperature (460 °C) deposition[31]. In general, the CSS system employs one-step deposition at a high temperature (e.g. 400–550 °C for CdTe) to achieve a suitable growth rate[29]. Due to the highly anisotropic nature of Sb_2Se_3, however, the low-temperature deposition is an imperative step to obtain a compact morphology. At the first deposition step of 340 °C, a compact thin film could be obtained, whereas an elongated 1D structure with incomplete coverage was observed when a

147 temperature of 460 °C was applied directly (Supplementary Fig. 2). Fig. 1a–c show the
148 microstructures of Sb_2Se_3 thin films deposited on an Au/FTO substrate by the two-step CSS
149 deposition process (i.e. successive depositions at 340 °C and 460 °C followed by cooling the
150 chamber naturally after deposition). The role of the Au layer in Sb_2Se_3 photoelectrodes, which
151 facilitates the transfer of photo-generated holes, has been discussed in previous reports on
152 Sb_2Se_3 for PEC water splitting[26,32] and thin-film solar cells[33]. Despite the film-type morphology,
153 there were some pin-holes resulting in exposure of the substrate (red circles in Fig. 1b) with
154 the faceted morphology of the Sb_2Se_3 thin films. Interestingly, it was found that a much
155 smoother pin-hole-free surface was achieved when N_2 gas was passed during the cooling
156 process after deposition under the same conditions (i.e. successive depositions at 350 °C and
157 450 °C), as shown in Fig. 1d–f. We denoted the sample prepared with N_2-assisted cooling as
158 the 'fast-cooling' sample, while the naturally cooled sample was denoted as the 'slow-cooling'
159 sample. The fast cooling sample revealed a slightly larger average value of grain size (~1038
160 nm) compared with the one of the slow cooling (~850 nm), while both samples had similar
161 standard deviation (~370 nm, Supplementary Fig. 3). The cooling rates for the fast cooling and
162 the slow cooling until it has reached 200 °C are approximately 15.7 °C/min and 11.3 °C/min,
163 respectively. In addition, the energy-dispersive X-ray spectroscopy (EDX) analysis showed
164 that both fast and slow cooling Sb_2Se_3 films are slightly selenium poor (Se/Sb ~ 1.35) as similar
165 with the previously reported CSS-Sb_2Se_3 thin films[31]. Fig. 1g shows the XRD data obtained
166 for both fast-cooling and slow-cooling samples: it reveals the preferred (hk1) orientations (i.e.
167 strong (211), (221), and (301) peaks with a negligible (120) peak (*pbnm space group*)). As
168 found in previous studies on Sb_2Se_3 thin-film solar cells, (hk1) orientations, representing
169 $(Sb_4Se_6)_n$ nanoribbons oriented perpendicular or inclined relative to the substrate (Fig. 1h, for
170 example), are advantageous for a superior performance owing to efficient carrier transport
171 along the [001] direction[18,19]. To quantify the relative intensities of each plane revealed in XRD

data to a standard Sb_2Se_3 powder (JCPDS 15-8601), we have calculated the texture coefficient T_c, which is defined as:

$$T_c(hkl) = n \frac{I(hkl)/I_o(hkl)}{\sum_1^n I(hkl)/I_o(hkl)}$$

where *I(hkl)* is the measured relative intensity of the peak corresponding to the *hkl* diffraction, $I_o(hkl)$ is the relative intensity from a standard powder sample (JCPDS 15-0861), and *n* is the total number of diffraction peaks used in the evaluation. A large T_c value for a specific diffraction peak indicates preferred orientation along this direction. In the present case, we chose four diffraction peaks (n = 4) corresponding to 2θ values of 120, 211, 221, and 301. Supplementary Fig. 4 clearly shows that T_c (120) of both fast and slow cooling samples is nearly zero while the other values are higher than 1, indicating both samples have (hk1) preferred orientation. Although both samples have a similar preferred orientation, it is also obvious that the fast cooling sample revealed higher T_c values of (211) and (301) planes and lower T_c value of (221) plane, implying possible rearrangement of the ribbons.

On comparing the morphological and crystallographic differences between the fast- and slow-cooling samples, it was obvious that the N_2 flow during the cooling process significantly affects the morphology and crystallographic orientation. As mentioned above, because Sb_2Se_3 has a strong 1D anisotropic nature, thermodynamically favourable sharp and facet morphologies are inevitably obtained when kinetically sufficient time is provided (i.e. slow cooling). In contrast, in case of fast cooling, which offers insufficient time to reach the thermodynamically stable morphology, a metastable smooth morphology can be achieved. This explanation is supported by the solution-processed Sb_2Se_3, in which 1D nanostructures were observed when sufficient Se precursor was provided, while the metastable planar type Sb_2Se_3 was obtained in Se-deficient conditions[27]. In addition, a slight change in XRD data implied that

the ribbons likely move during the cooling process, presumably due to the low melting temperature of Sb_2Se_3 (~608 °C). Thus, it can be reasonably concluded that in order to fabricate compact thin-film-type Sb_2Se_3 with favourably oriented $(Sb_4Se_6)_n$ ribbons, rearrangement of the ribbons should be kinetically suppressed as much as possible to prevent the formation of thermodynamically stable 1D structures. Obtained with kinetically controlled growth, it was possible to obtain Sb_2Se_3 thin films with a compact structure as well as well-oriented ribbons, both of which are expected to be favourable for better performance.

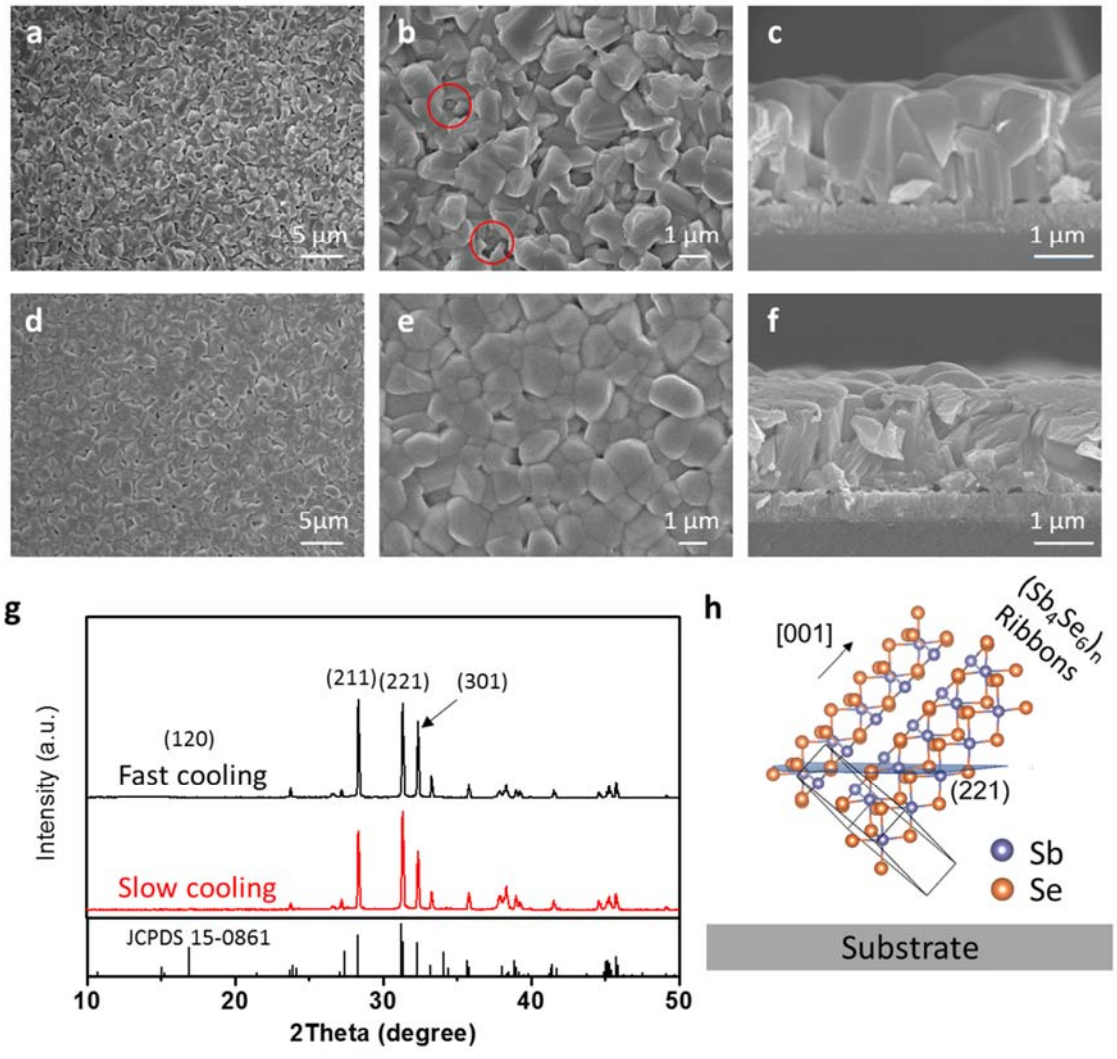

Fig. 1 | Microstructures and crystallographic orientation of Sb_2Se_3 thin films. a-f, SEM images of (a–c) slow-cooling Sb_2Se_3 and (d–f) fast-cooling Sb_2Se_3. **g,** XRD data for Sb_2Se_3

thin films. **h**, Schematic showing favourable orientation of $(Sb_4Se_6)_n$ ribbons. Source data used to generate this figure can be found in the Source Data file.

Photoelectrochemical performance of CSS-Sb_2Se_3 photocathodes

Fig. 2a–b show the PEC performance of $RuO_x/TiO_2/Sb_2Se_3$/Au/FTO photocathodes using fast-and slow-cooling Sb_2Se_3 films measured in pH 1 electrolytes. As we mentioned above, the Au layer acts as a hole selective contact, which facilitates the transfer of photo-generated holes while blocking the electrons backflow[32-33]. Without the Au layer, Sb_2Se_3 photocathodes revealed relatively poor performance while nearly similar morphology of Sb_2Se_3 was observed (Supplementary Fig. 5), which verifies the role of the Au layer not affecting the growth of Sb_2Se_3, but assisting the transfer of photo-generated charges. The RuO_x catalytic layer was deposited by the PEC method, while atomic layer deposition (ALD) was used for the TiO_2 layer, similar to a previous study[32]. In both samples, the onset potentials shifted towards a positive direction after the first scan due to activation of the RuO_x catalyst[34]. The photocurrent density of the fast-cooling sample approached 30 mA cm^{-2} at 0 V_{RHE}, which is not only the highest value obtained for a Sb_2Se_3 photocathode but also among the best observed for all photoelectrodes used in PEC water splitting so far. Note that the data shown in Fig.2 were obtained from the best performing device, while normally 25 – 30 cm^{-2} at 0 V_{RHE} photocurrent density was observed in the fast-cooling Sb_2Se_3 based photocathodes. Supplementary Fig. 6 shows the previously reported photocurrent densities of photoelectrodes for PEC water splitting under short circuit conditions (i.e. 1.23 V_{RHE} for photoanode and 0 V_{RHE} for photocathode) plotted with the theoretical maximum photocurrent density as a function of the band gap of the semiconductor materials. Although the photocurrent density of some large-E_g semiconductors such as TiO_2, WO_3, and GaP has reached the theoretical maximum, it has

229 remained below 10 mA cm^{-2} in such cases due to their large E_g. One of the highest photocurrent
230 density values was achieved by a p-type Si based photocathode (~35.5 mA cm^{-2} at 0 V_{RHE})[35].
231 However, considering the small band gap of Si (~1.1 eV) and the established history of the Si-
232 based industry, the high photocurrent density obtained by the Si photocathode does not
233 represent a remarkable result. Moreover, due to the low α of crystalline Si, complex microwire
234 structures with sufficient thickness (p-Si wafer of 525 μm and Si microwires of 40 μm) and
235 high-purity single-crystals are indispensable for an efficient Si photocathode. In addition to the
236 Si photocathodes, a high photocurrent of ~30 mA cm^{-2} at 0 V_{RHE} was exhibited by the thin (1–
237 1.5 μm) and polycrystalline p-Cu(In,Ga)Se_2 photocathode[36]. Despite the high photocurrent
238 density, however, the use of expensive In and Ga could be a major bottleneck for the fabrication
239 of large-area specimens. Given the low-cost and relatively short history of Sb_2Se_3 as well as
240 the simple preparation and low material usage due to the high α, the high photocurrent density
241 of ~30 mA cm^{-2} at 0 V_{RHE} clearly demonstrates the strong potential of Sb_2Se_3 as a promising
242 photocathode material. It is worth emphasizing that the most important building block in a PEC
243 water splitting device in terms of cost-effectiveness is the light-absorbing semiconductors. For
244 example, the cost portion of electrocatalysts in the c-Si based PV-EC system is just
245 approximately 1 % (whether the electrocatalyst is Ir-Ru or NiFe-NiMo) for overall cost of
246 hydrogen production [37]. Additionally, in the high STH systems based on III–V semiconductors,
247 the cost of InGaP/GaAs ($175) per unit solar collection area is much greater than other parts
248 such as catalysts (Pt and IrO_x, $8) and membranes (127 mm-thick Nafion, $5)[38]. Moreover, the
249 community is recognizing that noble metals are easy to recycle, as well as price of hydrogen
250 expected from non-noble metal electrocatalysts is not competitive to the one with noble metal
251 ones[39]. Thus, despite the use of relatively expensive catalysts and a hole selective contact layer,
252 the high performance of our device demonstrates the feasibility of cost-effective Sb_2Se_3 based
253 photoelectrodes for PEC water splitting.

While the fast-cooling sample revealed a record photocurrent density, the photocurrent density of the slow-cooling sample with a RuO_x co-catalyst, which had a facet morphology, was relatively low (~17 mA cm^{-2} at 0 V_{RHE}, Fig. 2b). Fig. 2c exhibits the half-cell solar-to-hydrogen conversion efficiencies (HC-STH) calculated from the 3rd scans in Fig. 2a–b according to the equation HC-STH = $I_{ph} \times (E_{RHE} - E_{H+/H2})/P_{SUN} \times 100\%$, where I_{ph} is the photocurrent density obtained under an applied bias of E_{RHE}, $E_{H+/H2}$ is 0 V_{RHE}, and P_{SUN} is 100 mW cm^{-2}. It is worth noting that the maximum value of HC-STH in the fast-cooling was is observed at a more positive potential of 0.16 V_{RHE} compared with that of the slow-cooling counterpart (0.09 V_{RHE}), indicating that the fast cooling strategy is advantageous for not only the photocurrent, but also the photovoltage and fill factor. As shown in Fig. 2d, both fast- and slow-cooling Sb_2Se_3 photocathodes were able to harvest photons over 1000 nm, but the IPEC was much higher for the fast-cooling sample over the entire wavelength. Because the optical properties (e.g. surface reflection of Sb_2Se_3/Au/FTO samples) for the fast- and slow-cooling samples were nearly identical (Supplementary Fig. 7), optical properties can be excluded from the potential origin of the difference noted in the performance. In addition, a similar performance was observed when a Pt co-catalyst was used (Pt/TiO_2/Sb_2Se_3/Au/FTO, Supplementary Fig. 8): thus, we can conclude that the performance difference arose not from the co-catalyst, but presumably from the TiO_2/Sb_2Se_3 junction.

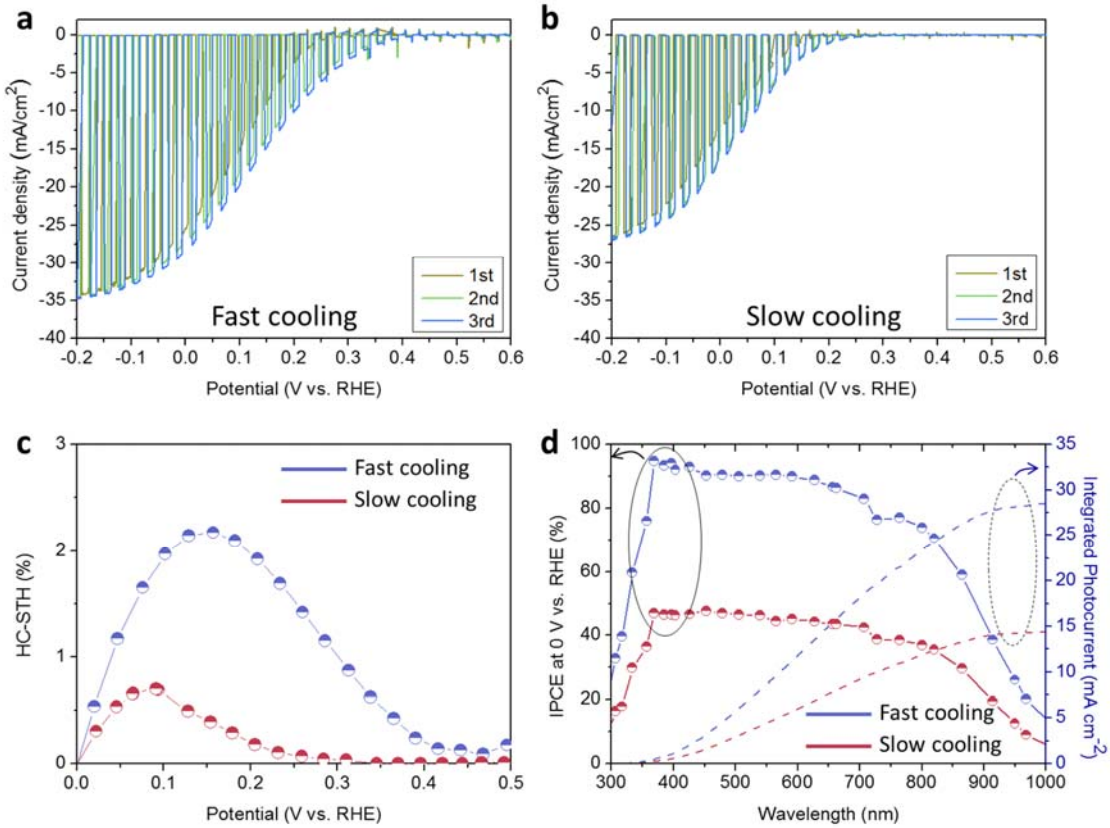

Fig. 2. | PEC performance of $RuO_x/TiO_2/Sb_2Se_3$/Au/FTO photocathodes in pH 1 H_2SO_4 electrolyte. a-b, J–V curves of (a) fast- and (b) slow-cooling samples under simulated 1 sun air mass 1.5 G chopped illumination at a scan speed of 5 mV s^{-1} from positive to negative potential and **c,** corresponding HC-STH efficiencies. **d,** Wavelength-dependent IPCE and integrated photocurrent density of fast- and slow-cooling samples measured at 0 V_{RHE}. Source data used to generate this figure can be found in the Source Data file.

In order to understand the performance difference observed for the fast- and slow-cooling samples, we performed Kelvin probe force microscopy (KPFM) analyses, which allowed us to investigate the topography and surface potential distribution. Fig. 3a,c and b,d show the surface topography and surface potential of TiO_2/Sb_2Se_3 devices, respectively. The fast-cooling TiO_2/Sb_2Se_3 revealed relatively uniform distribution of surface topography and potential, as shown in Fig. 3a–b. On the other hand, some noticeable high-potential regions, as represented by the bright yellow colour in Fig. 3d, were observed for the slow-cooling

TiO_2/Sb_2Se_3 sample. Topography and potential line profiling for the fast-cooling sample suggested that the potential resembles the topography of TiO_2/Sb_2Se_3 (Fig. 3e), indicating a lower surface potential at the grain boundaries of Sb_2Se_3[40]. In the fast-cooling sample, the separation of the photo-generated electrons and holes efficiently occurred along the vertically aligned $[Sb_4Se_6]_n$ ribbons, as shown in Fig. 3g, owing to the p–n junction and relatively small lateral potential difference. In contrast, in the slow-cooling sample, the surface potential increased significantly with a rapid drop in the topography (Fig. 3f), indicating direct contact between the n-type TiO_2 layer and substrate due to pin-holes. It might be worth to note that the height recorded by AFM and KPFM ranged from a few nm to hundreds nm and even sometimes μm scale[41-42]. In such a case, the photo-excited electrons can be extracted laterally to the ribbons and they can recombine with the holes at the back contact as shown in Fig. 3h due to the large electric field across the p–n junction. It is widely known that direct contact between the top and bottom contact can cause significant degradation of the performance, even in the case of the chemical composition and optoelectronic properties have negligible differences. For example, Luo et al. reported the effect of a thin blocking layer to prevent shunt pathways, thereby enabling much higher performance in Cu_2O nanowire photocathodes without any noticeable differences in chemical composition and morphology[43]. The KPFM results clearly demonstrated the importance of pin-hole-free compact thin films in preventing the recombination and the performance degradation mechanism in the presence of pin-holes, which had not yet been experimentally demonstrated. ~~as well as the origin of the performance difference between the fast- and slow-cooling samples.~~

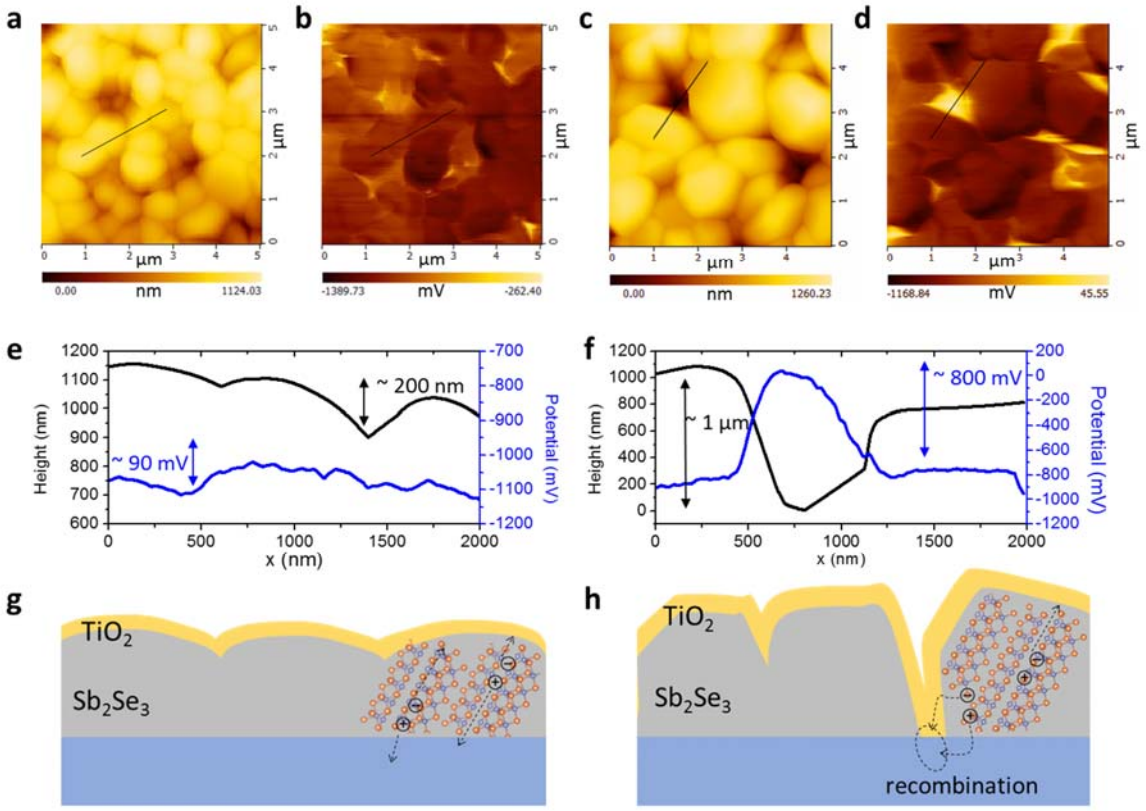

Fig. 3. | Topography and surface potential of TiO_2/Sb_2Se_3 according to KPFM analysis. a, c, Topography of (a) fast- and (c) slow-cooling samples. **b, d,** Surface potential of (b) fast- and (d) slow-cooling samples. **e, f,** Topography and potential line profile (obtained from scanning the black lines in Fig. 3a–d) for (e) fast- and (f) slow-cooling samples. **g, h,** Schematics showing possible charge separation and recombination in (g) fast- and (f) slow-cooling samples. Source data used to generate this figure can be found in the Source Data file.

Sb_2Se_3 photocathodes in unassisted water splitting

Despite the high photocurrent density of the fast-cooling CSS-Sb_2Se_3 photocathodes, there remain some issues prior to achieving unassisted water splitting by fabricating a tandem device in conjunction with the photoanode. The primary crucial issue is electrolyte compatibility because most of the efficient photoanodes reveal high performance in a near-neutral electrolyte,

while our Sb_2Se_3 photocathodes were tested in harsh acidic electrolytes. We measured the PEC performance of our fast-cooling Sb_2Se_3 photocathode with two different co-catalysts, Pt and RuO_x, in both acidic (Supplementary Fig. 9a) and neutral (Supplementary Fig. 9b) electrolytes. In the acidic electrolyte, both RuO_x and Pt co-catalysts exhibited the same onset potential whereas a lower photocurrent density was observed in the Pt-coated sample. The lower photocurrent in the Pt co-catalyst sample was attributed to less light absorption and reflection by Pt nanoparticles, which is often quoted as a major issue associated with the use of Pt co-catalysts in the PEC system[44]. A more delicate strategy for depositing Pt co-catalyst uniformly, such as the two-step platinisation method[45], could boost the performance of our $Pt/TiO_2/Sb_2Se_3$ photocathodes. Another interesting difference between RuO_x and Pt was the stability. The $RuO_x/TiO_2/Sb_2Se_3$ sample retained approximately 60% of initial photocurrent density after 35 hours in the neutral electrolytes, which is the best stability of Sb_2Se_3 photocathodes reported so far (Supplementary Fig. 10a). The photocurrent density of $Pt/TiO_2/Sb_2Se_3$ decreased more rapidly (42% photocurrent after 5 h), probably due to the larger bubbles at Pt surfaces, as evidenced by severe fluctuations in the enlarged photocurrent curves (Supplementary Fig. 10b–c). It should be noted that the detachment of Pt particles due to the releasing of large bubbles is one of the well-known degradation mechanisms in the Pt-decorated photocathodes for water splitting[46]. We measured Raman spectroscopy to investigate the chemical composition variation after the reliability test. Before the stability test, the Raman spectra of the $RuO_x/TiO_2/Sb_2Se_3/Au/FTO$ photocathode showed one distinct peak at ≈ 190 cm^{-1} along with a shoulder peak at ≈ 208 cm^{-1}, both of which are attributed to the vibration modes in Sb_2Se_3 phase (Supplementary Fig. 11a). After the stability test, an additional peak located at ≈ 250 cm^{-1} appeared. The additional peak indicates the formation of by-products such as Sb_2O_3 (≈ 254 cm^{-1}) and/or several Se phases (e.g., Se_8 rings at ≈ 253 cm^{-1}, Se_6 rings at ≈ 247 cm^{-1}, and amorphous Se at ≈ 250 cm^{-1}) as a result from the decomposition of Sb_2Se_3. In addition, there

345 was also morphological destruction after the stability test (Supplementary Fig. 11b-c).
346 According to our previous study on the stability of Sb_2Se_3 photocathodes[25], the morphological
347 destruction of Sb_2Se_3 photocathode is caused by the photo-reduction of TiO_2 accompanied by
348 the degradation of Sb_2Se_3. Despite the high photocurrent density and high stability of the RuO_x
349 sample, it resulted in a smaller onset potential compared with that owing to the Pt sample due
350 to the low catalytic activity of RuO_x in a neutral electrolyte (Supplementary Fig. 9b). As the
351 onset potential is an important metric for determining the operating point in PEC tandem device,
352 we decided to use a Pt co-catalyst for the PEC tandem device.

353 With the Pt co-catalyst, we inserted a CdS layer between TiO_2 and the fast-cooling
354 Sb_2Se_3 to further enhance the onset potential, as shown in Fig. 4a[27]. The thickness of the CdS
355 and TiO_2 layers were approximately 50 nm and 30 nm, respectively (Supplementary Fig. 12).
356 Upon deposition of the CdS layer, the onset potential of the Sb_2Se_3 photocathode shifted up to
357 0.5 V_{RHE} and the fill factor was also significantly enhanced (Fig. 4b). As a result, the maximum
358 HC-STH increased from 2.33% to 3.4%, and the potential at which the maximum HC-STH
359 was observed also shifted from 0.18 V_{RHE} to 0.26 V_{RHE}, as shown in Fig. 4c. Therefore, despite
360 the slightly decreased photocurrent density at 0 V_{RHE}, Pt/TiO_2/CdS/Sb_2Se_3 configuration was
361 more suitable for the PEC tandem device. The enhanced onset potential and fill factor could be
362 attributed to the reduced band mismatch between TiO_2 and Sb_2Se_3[27]. Fig. 4d shows the incident
363 photon to current conversion efficiency (IPCE) spectra for Sb_2Se_3 photocathodes with and
364 without CdS layers, suggesting that the IPEC of 300–500 nm decreased with the thickness of
365 the CdS layer. The reduced IPCE values imply that the photons absorbed by the CdS ($E_g \sim 2.4$
366 eV, ~516.6 nm) were unable to contribute to the photocurrent density. Therefore, when the
367 thickness of the CdS layer increased, the photocurrent density decreased whereas the onset
368 potential remained as the same (i.e. ~ 0.5 V_{RHE}), indicating the necessity of careful optimisation
369 of the CdS layer thickness (Supplementary Fig. 13).

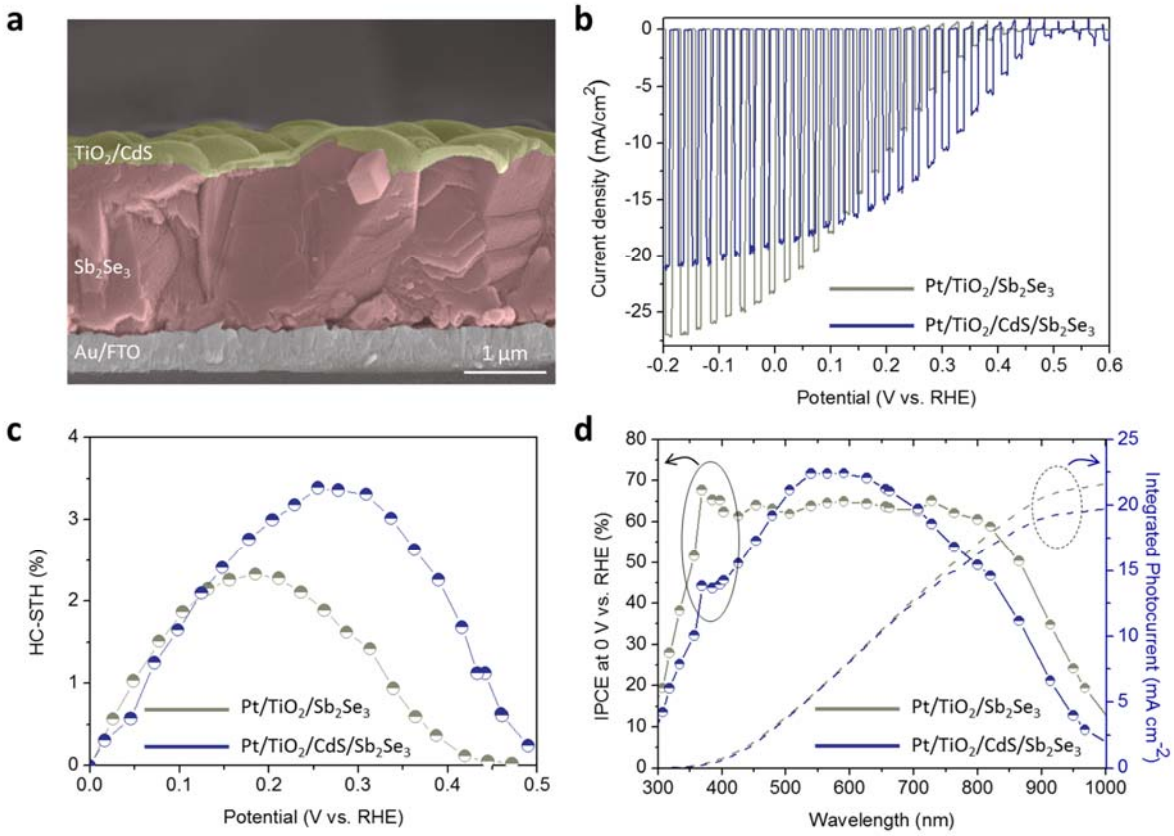

Fig. 4. | Microstructure and PEC performance of $Pt/TiO_2/CdS/Sb_2Se_3/Au/FTO$ photocathodes. a, Cross-sectional SEM image of $TiO_2/CdS/Sb_2Se_3$ on Au/FTO substrate. **b,** J–V curves for Sb_2Se_3 photocathodes with/without a CdS layer in pH 1 H_2SO_4 under simulated 1 sun air mass 1.5 G chopped illumination at a scan speed of 5 mV s^{-1} from positive to negative potential and **c,** corresponding HC-STH efficiencies. **d,** Wavelength-dependent IPCE at 0 V_{RHE} of Sb_2Se_3 photocathodes with/without CdS layer. Source data used to generate this figure can be found in the Source Data file.

Photocathode–photoanode D4 tandem cell for unbiased solar overall water splitting

Since the band gap of Sb_2Se_3 is 1.2 eV, which is suitable for realising a D4 tandem cell as a bottom electrode with a different top light absorber[47], we fabricated tandem cells coupled with $BiVO_4$-based photoanodes (E_g ~ 2.4 eV), which have been widely used for high-performance

photocathode–photoanode tandem cells[10] (Fig. 5a). The H,Mo:$BiVO_4$ photoanode used here revealed good transparency (Supplementary Fig. S14) and performance (~4.7 mA cm^{-2} at 1.23 V_{RHE} and onset potential of 0.25 − 0.3 V_{RHE}) as a top light absorber. To achieve high efficiency, further optimisation of the electrolyte was conducted for the tandem cell comprising two photoelectrodes involving opposite reactions. We tested various concentrations of phosphate buffer (0.1–1.0 M) to investigate its effect on the photocathode (Supplementary Fig. 15) and photoanode (Supplementary Fig. 16). For the Sb_2Se_3 photocathode, because the surface charge transfer kinetics is governed by Pt and photovoltage is achieved by the buried junction (i.e. TiO_2/CdS/Sb_2Se_3), a more conductive (higher concentration) electrolyte showed better performance[48]. On comparing Pt/TiO_2/CdS/Sb_2Se_3/Au/FTO and Pt/FTO, they exhibited an almost linear dependence of photocurrent density on the concentration of phosphate buffer (Supplementary Fig. 15d). Onset potential of the two (photo)electrodes (i.e. Pt/FTO and Pt/TiO_2/CdS/Sb_2Se_3/Au/FTO) showed negligible change while the current density varied greatly; from the concentration of 0.1 M to 0.5 M, the Sb_2Se_3 photocathode revealed a three-fold increment while the Pt electrocatalyst showed a five-fold increase in the current density. However, at a high concentration of 1.0 M, the stability of the photocathode degraded presumably due to the accelerated Pt detachment in the higher photocurrent condition. (Supplementary Fig. 15c), so that 0.5 M could be a judicious choice for the photocathode considering both the photocurrent and the stability. For the photoanode, the completely opposite tendency was observed: the photocurrent of $NiFeO_x$/FTO (as an electrocatalyst) showed a linear dependence on the concentration, but that of $NiFeO_x$/$BiVO_4$/FTO (as a photoanode) revealed almost no dependence on the electrolyte concentration (Supplementary Fig. 16). This is due to the working mechanism of $NiFeO_x$/$BiVO_4$, which formed an adaptive junction with water-permeable $NiFeO_x$ showing two different effects of 1) passivation and 2) alternative active sites for improving the surface hole transfer[49,50]. Therefore, for the

concentrations we tested (0.1–1.0 M), no photocurrent enhancement occurred for a higher concentration for the $NiFeO_x/BiVO_4$ photoanodes, so that the use of higher concentration of electrolyte had no beneficial effect. In fact, a higher electrolyte concentration could assist the corrosion of the electrocatalyst and photoanode (dissolution of $BiVO_4$ in phosphate buffer is spontaneous and accelerated by surface photo oxidation[51]). Therefore, it would be desirable to use a 0.5 M phosphate buffer as an operating electrolyte that provides moderately benign conditions for both photoelectrodes. However, owing to the low stability of $BiVO_4$ in phosphate, fast degradation of performance was observed for the tandem cell, and we addressed the stability issue by adding vanadium cation (V^{5+}) as done by Choi group[52]. It should be noted that theoretically the V^{5+} can be reduced prior to proton, possibly affecting the performance of our Sb_2Se_3 photocathode-based tandem devices for water splitting. As shown in Supplementary Fig. 17a, there are distinctive peaks in the LSV scans for a Pt electrode upon addition of V^{5+} into strongly acidic electrolyte, indicative of a significant reduction of V^{5+}. In contrast, there is no noticeable difference between with/without V^{5+} electrolyte when measured in a neutral electrolyte (0.5 M KPi, Supplementary Fig. 17b). These results imply that the reactivity of V^{5+}, which is relatively stronger in an acidic electrolyte, significantly decreases in a neutral electrolyte. As we measured our Sb_2Se_3-based tandem device in a neutral electrolyte (0.5 M KPi), there is no significant change of both the Sb_2Se_3 photocathode and the $BiVO_4$ photoanode upon adding V^{5+} into our electrolyte as shown in Supplementary Fig. 18. It is also noteworthy that the slight difference observed in the photocathode case (Supplementary Fig. 18d), possibly due to parasitic light absorption by yellow V^{5+} ions, does not affect the performance of our tandem device as the operation potential of the tandem device is around 0.4 V_{RHE}. Accordingly, in any cases, it is reasonable to conclude that addition of V^{5+} does not interfere with the hydrogen production by our Sb_2Se_3-based tandem device.

As shown in Fig. 5b, the operating point of the two photoelectrodes, as estimated by the intersection of two J–V curves, was approximately 1.2 mA cm^{-2} at 0.4 V_{RHE}, which corresponded to a STH efficiency of 1.5%. It should be noted that photocurrent density of $BiVO_4$ at 0.4 V_{RHE} varies from 1.2 to 0.8 mA cm^{-2}, thus the overall STH efficiencies of the tandem cell range from 1.48 % to 0.98 %. In addition, the polarisation curves of $BiVO_4$–Pt (as the counter electrode) and $BiVO_4$–Sb_2Se_3 (as the counter electrode) demonstrated a ~0.5 V anodic shift induced by the Sb_2Se_3 photocathode, indicating that the Sb_2Se_3 photocathode provided a photovoltage of 0.5 V (Fig. 5c). The $BiVO_4$–Sb_2Se_3 tandem cell exhibited 1.2 mA cm^{-2} at 0 V against the counter electrode (i.e. unbiased conditions), which was in agreement with the estimated value according to the overlapped J–V curves shown in Fig. 5b. This observation verified that the total photovoltage of 1.45 V (0.52 V from the Sb_2Se_3 photocathode and 0.93 V from the $BiVO_4$ photoanode) was sufficient to implement unbiased overall water splitting, resulting in evolution of both H_2 and O_2, by overcoming the thermodynamic potential requirement (1.23 V). In comparison to previously reported photoelectrodes, the total photovoltage of 1.45 V was a moderate value considering the band gap energies[53]. Thus, it is noteworthy that a photovoltage increment of ~0.1 V and the enhanced fill factor obtained using CdS played a critical role in driving the overall water splitting.

Photon utilisation capability of the $BiVO_4$–Sb_2Se_3 tandem cell was confirmed by IPCE measurements. For $BiVO_4$, photons up to ~510 nm (E_g of 2.45 eV) could be converted and the absorption current density, which represents the maximum photocurrent density under the absorbance of $BiVO_4$, was calculated to be 5.5 mA cm^{-2} (Supplementary Fig. 10d). Sum of the photon flux before and after passing through $BiVO_4$ up to the wavelength of 1033 nm (~1.2 eV, E_g of Sb_2Se_3) was calculated to be 39.9 and 24.4 mA cm^{-2}, respectively, which are much higher than the photocurrent of $BiVO_4$ at the top of the tandem cell configuration.

We compared $BiVO_4$ and Sb_2Se_3 in two different bias conditions: 1) high bias near short circuit of the individual photoelectrode (1.0 V_{RHE} for photoanode and 0.1 V_{RHE} for photocathode) (Supplementary Fig. 19) and 2) operating bias at 'actual' operating point (0.4 V_{RHE} for both the photocathode and photoanode) (Fig. 5d). In both cases, a broad range of photons could be effectively utilised by the synergetic effect of $BiVO_4$ (to 510 nm) and Sb_2Se_3 (from 450 to 1000 nm). In case of the high bias condition, both the photocathode and photoanode showed a quite high IPCE (~70% at 450 nm for $BiVO_4$ and ~60% for Sb_2Se_3). The photocurrent calculated from the IPCE was 3.2 mA cm^{-2} for the $BiVO_4$ photoanode. In addition, the photocurrent of the Sb_2Se_3 photocathodes was 18.5 mA cm^{-2} and 10.3 mA cm^{-2} with or without $BiVO_4$, respectively. These values are in a good agreement with photocurrents shown in the J–V curves (Supplementary Fig. 18). On the other hand, as expected, a lower IPCE was observed under the operating bias (0.4 V_{RHE}): ~25% at 450 nm for $BiVO_4$ and ~15% for Sb_2Se_3, as shown in Fig. 5d. The photocurrent density calculated using the IPCE spectra of $BiVO_4$ at 0.4 V_{RHE} was about 1.1 mA cm^{-2}, which is similar to the values shown by the J–V curve (Supplementary Fig. 18). However, the photocurrent density of Sb_2Se_3 photocathodes at 0.4 V_{RHE} with and without $BiVO_4$ were 5.0 mA cm^{-2} and 2.2 mA cm^{-2}, respectively, which are higher than the photocurrents shown by the J–V curve. This discrepancy between the photocurrent density at 0.4 V_{RHE} demonstrated by the IPCE and J–V curve can be attributed to the light-intensity-dependent carrier mobility of Sb_2Se_3. As the carrier mobility of Sb_2Se_3 is much higher under low-intensity light[32], Sb_2Se_3 photocathodes showed a better fill factor in IPCE measurement conditions (~100 μW cm^{-2}) compared with the 1 sun conditions (100 mW cm^{-2}), thereby resulting in a higher photocurrent according to the IPCE spectra at 0.4 V_{RHE}. The D4 tandem cell consisting of Sb_2Se_3 and $BiVO_4$ operated stably for over 10 h without any noticeable degradation in the photocurrent density (Fig. 5e). The efficiency and stability of our Sb_2Se_3-based tandem cells are comparable to those of the best-performing tandem cells

containing other types of photocathode materials (vide infra). Finally, a larger tandem cell was constructed using a $BiVO_4$ photoanode (0.81 cm^{-2}) and a Sb_2Se_3 photocathode (0.35 cm^{-2}) under simulated ~3 sun, which clearly demonstrated a constant generation of O_2 and H_2 gas evolution (Supplementary video 1, Supplementary Fig. 20).

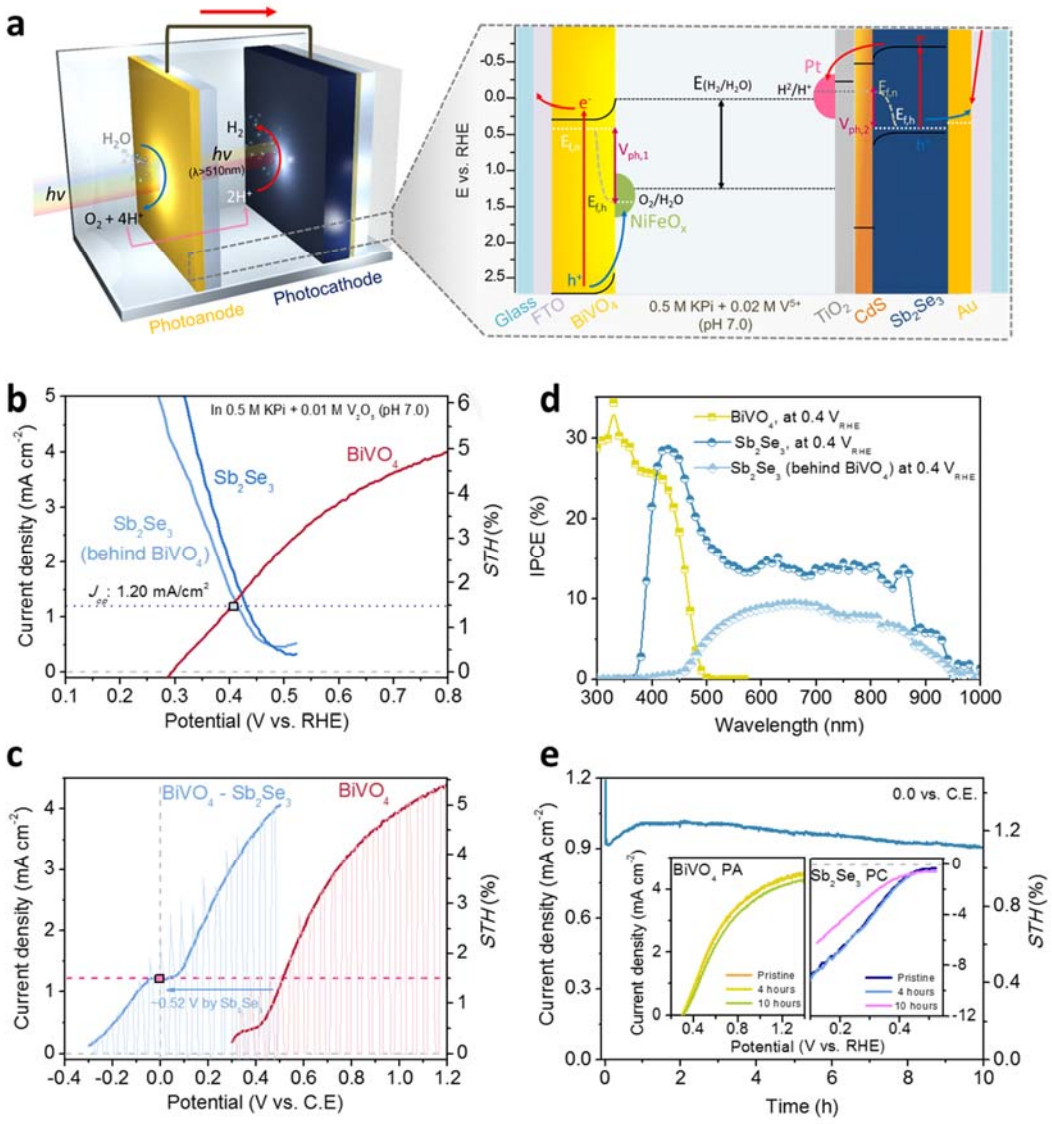

Figure 5| Sb_3Se_3 photocathode−$BiVO_4$ photoanode for solar overall water splitting PEC cell. a, Scheme of the $NiFeO_x$/H,Mo:$BiVO_4$/FTO–Pt/TiO_2/CdS/Sb_2Se_3/Au/FTO tandem cell operating in pH 7.0 phosphate buffer. **b,** *J–V* curve for the photocathode and photoanode; the

operating point is marked for the tandem cell (photoelectrode active area: 0.32 cm^2). **c,** Two-electrode measurements for photoanode–counter electrode (C. E.) and photoanode–photocathode tandem cells (active area: 0.28 cm^2). **d,** IPCE at 0.4 V_{RHE} measured for the photoanode and photocathodes. **e,** Photocurrent generation under short circuit conditions (0 against counter electrode) of the photoanode–photocathode tandem cell. All analyses were conducted in 0.5 M phosphate buffer + 0.01 M V_2O_5 (pH 7.0) at a scan rate of 20 mV s^{-1}. Distance between the photoanode and photocathode was ~0.5 cm. Source data used to generate this figure can be found in the Source Data file.

Even though we report herein the first demonstration of unbiased water splitting using a Sb_2Se_3 photocathode in a single reactor, better tandem cell systems are likely achievable by 1) using two different electrolytes that are separately optimised for each photoelectrode (e.g. pH 1 for Sb_2Se_3 and pH 9 borate for $BiVO_4$) along with a bipolar membrane[35] or 2) stabilising both the photocathode and photoanode using additives (e.g. chelating agent to deter poisoning) in the electrolyte[54]. Bearing in mind its short history and potential for further enhancement, the performance of the Sb_2Se_3-based tandem cell (STH efficiency of 1.5% and stability of over 10 h) is quite remarkable particularly in comparison with previously reported results for photocathode–photoanode tandem cells[4] (Fig. 6a, Table S1 in Supplementary Information). We categorised the tandem cells based on the bottom light absorbers (silicone based, III-V, Cu-chalcogenides, metal oxides and perovskites). Most of them used $BiVO_4$, which is currently the most suitable photoanode material and ensures good transparency (~80% beyond photon utilisation threshold (~520 nm))[10]. It was found that the efficiency of the $BiVO_4$–Sb_2Se_3 tandem cell (1.5% STH) was not the highest when compared to that of $BiVO_4$–CIGS (3.7%)[48], $BiVO_4$–Cu_2O (3.0%)[55], and $BiVO_4$–c-Si (2.1%)[35]. Considering the cost of materials (much lower than that of CIGS), small band gap (compared to that of Cu_2O, E_g ~ 2.0 eV), simple preparation, and low material usage (compared to that of Czochralski-grown Si wafer and complicated Si microwires), the >1% STH can be considered a significant milestone for PEC tandem cells. Moreover, 10 h of stability is also the best result reported for photoanode–photocathode tandem

cells except for the 20 h stability achieved by the expensive CIGS-based photocathodes[56] (Fig. 6b). The exceptional performance and stability of the Sb_2Se_3 photocathode presented here, as well as several desirable material characteristics of Sb_2Se_3 such as its high α, optimal band gap of ~1.2 eV, and comparable photovoltage to that of c-Si (~0.5 V), clearly present a promising pathway towards realising a competitive overall water splitting PEC cell system, which could potentially result in a STH of approximately 10% using $BiVO_4$ photoanodes, whose E_g is 2.4 eV (Supplementary Fig. 21a). In order to demonstrate a higher STH efficiency, the areas of focus should include enhancing both the photovoltage and fill factor through interface engineering, such as the recently reported dipole engineering at the buried junction.[57] In addition, the development of an ideal photoanode material with an E_g close to 1.8 eV could potentially enable a STH efficiency of over 20% on using the Sb_2Se_3 photocathode (Supplementary Fig. 21b). Although the value of STH 1.5% is not superior in comparison to that of other systems, such as photovoltaic–electrolytic systems (average 10–20%), buried-junction photoelectrodes (10–15%), and photovoltaic–PEC systems (3–8%), because of the simplicity of the photoanode–photocathode system, the price of hydrogen produced from such a system will be lower. Therefore, not only the STH efficiency but also the cost should be considered when comparing such systems. The reported STH efficiencies of the photoanode–photocathode tandem system are increasing very rapidly (Fig. 6), which suggests increasing research interest in reducing the complexity of overall water splitting devices[4].

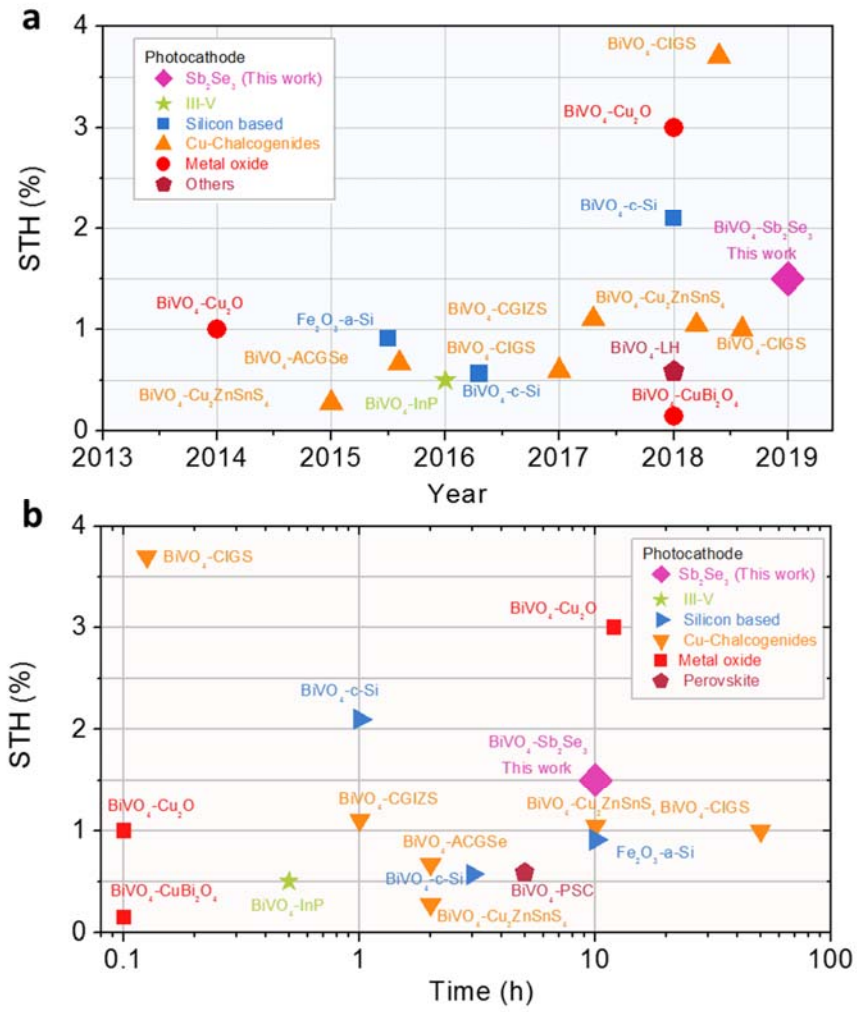

Fig. 6 | Efficiency and stability benchmarks for photoanode–photocathode D4 tandem cell. **a,** Solar-to-hydrogen efficiencies reported in recent years and **b,** their operation duration. All reports are summarised in Supplementary Table S1.

~~Conclusion~~

In conclusion, we have demonstrated a high-performance photocathode using an earth-abundant Sb_2Se_3 semiconductor, which has a small Eg (~1.2 eV), good optoelectronic properties, and no secondary phase. By suppressing the growth kinetics during the CSS

deposition, a compact and pinhole-free Sb_2Se_3 thin film was obtained, which enabled a highest photocurrent density of up to 30 mA cm^{-2} by avoiding recombination and accelerating charge separation through well-aligned $(Sb_4Se_6)_n$ ribbons. Inserting a CdS layer between Sb_2Se_3 and TiO_2 increased the onset potential and consequently improved the HC-STH efficiency up to 3.4%. Finally, by combining the material with a $BiVO_4$ photoanode, unbiased overall water splitting was achieved with impressive efficiency (~1.5%) and high stability of 10 h. These performances and stability significantly surpass those of previously reported Sb_2Se_3 photocathodes and are comparable to those of other expensive thin film photocathodes. Given the relatively short history of photoelectric materials, it is expected that rapid progress of Sb_2Se_3 photocathodes will lead to better efficiency in the near future and our findings represent an important demonstration of a photocathode–photoanode-based PEC device. We believe that the emerging Sb_2Se_3 substrate can be an attractive breakthrough material for practical solar fuel production.

Methods

Preparation of Sb_2Se_3 thin films

Sb_2Se_3 films were deposited via a two-step CSS process[31] using a custom-made CSS system. First, a compact layer was grown from stoichiometric Sb_2Se_3 (Alfa Aesar, 99.999% metals basis) using a source temperature of 340 °C and a substrate temperature of 390 °C for 2 min at a pressure of 0.05 mbar. Subsequently, deposition was completed using a source temperature of 460 °C for 15 min and a pressure of 13 mbar. These films were then cooled either slowly or fast, by turning the heater off and flowing N_2 over the sample at a rate of either 0 or 5 L min^{-1}, respectively.

Deposition of overlayers and catalysts for Sb_2Se_3 photocathodes

CdS layers were deposited by the chemical bath deposition (CBD) method. Prior to CBD, the sample was pre-treated in a bath containing a solution of $CdSO_4$ (Sigma Aldrich, 99.99%) and NH_4OH (Duksan, 28 wt%) at 60 °C for 10 min. CBD of CdS was performed by immersing the pre-treated sample in a solution containing $CdSO_4$, thiourea (99%, Sigma Aldrich), deionised water, and NH_4OH for 5 min at 60 °C. TiO_2 layers were deposited using an ALD system (Lucida D100, NCD Inc.). The ALD process was performed at 150 °C, with tetrakis(dimethylamido)titanium (TDMAT) and H_2O as the Ti and O sources, respectively. A total of 600 ALD cycles were carried out, each of which comprised a TDMAT pulse of 0.3 s followed by 15 s of N_2 purging and a H_2O pulse of 0.2 s followed by 15 s of N_2 purging. The approximate growth rate of TiO_2 was 0.55 Å per cycle, as estimated using an ellipsometer. The Pt catalyst was sputtered onto the TiO_2-coated Sb_2Se_3 electrode using an Auto Sputter Coater (Ted Pella, Redding, CA, USA) under an applied current of 10 mA for 120 s. A galvanostatic photo-deposition technique was used for RuO_x deposition. The prepared photoelectrodes were immersed in a 1.3 mM solution of $KRuO_4$ at a current density of –28.3 μA cm^{-2} for 15 min under simulated 1 sun illumination.

Preparation of $BiVO_4$ films

All chemicals used in this study were of analytical grade and used without further purification. $BiVO_4$ film was prepared by a modified metal–organic decomposition (MOD) method according to our previously reported procedure[58] with slight modifications. In brief, 291 mg of $Bi(NO_3)\cdot 5H_2O$ (99.8%; Kanto Chemicals) and 163 mg of $VO(acac)_2$ (98.0%; Sigma Aldrich) were dissolved in 15 mL of acetyl acetone (>99.0%; Kanto Chemicals). As the dopant solution, 0.03 M $MoO_2(acac)_2$ (98.0%; Sigma Aldrich) in acetyl acetone (>99.0%; Kanto Chemicals) was prepared. A 0.2 M $Bi(NO_3)\cdot 5H_2O$ (99.8%; Kanto Chemicals) solution dissolved in acetic

598 acid (>99.0%; Kanto Chemicals) was used to compensate the Mo precursor-added solution.
599 For Mo doping, a Bi:(V+Mo) = 1:1 atomic ratio was used for preparing the 1% Mo:$BiVO_4$
600 films. To fabricate the $BiVO_4$ film, 35 μL of the solution was dropped on a FTO glass sample
601 (2 cm × 2.5 cm) and dried for 10 min in Ar atmosphere. The FTO glass (TEC 8; Pilkington)
602 was cleaned using ethanol + 35 wt% H_2O_2 (Samchun Chemical) used in a ratio of 5:1 under
603 sonication (~20 min) and washed with copious amounts of ethanol and finally stored in 2-
604 propanol before use. The greenish transparent precursor film was calcined at 550 °C for 30 min
605 to form a yellow $BiVO_4$ film. After annealing process, the 2 cm × 2.5 cm $BiVO_4$/FTO was split
606 to obtain photoanodes with a net irradiation area of 0.36 cm^2 connected by silver paste and
607 copper wire and sealed with epoxy resin.

608 ***Hydrogen treatment of metal oxide films***

609 Hydrogen treatment was conducted using the borohydride decomposition method reported by
610 Hao *et al*.[59] First, 16 mmol of $NaBH_4$ (>98%; Sigma Aldrich) was introduced in a 200 mL
611 alumina crucible and another smaller alumina bottle (15 mL) was introduced to the $NaBH_4$
612 powder. In this smaller bottle, an as-prepared metal oxide film (2 cm × 2.5 cm) was placed and
613 finally the 200 mL alumina crucible was covered with an alumina cover. This reactor was
614 placed in an already-heated furnace at 500 °C for 30 min. Then, the crucible was taken out
615 from the furnace and cooled naturally.

616 ***$NiFeO_x$ co-catalyst deposition on $BiVO_4$ film***

617 The $NiFeO_x$ co-catalysts were deposited by photo-assisted electrodeposition (PED) under AM
618 1.5G illumination according to a reported procedure[60]. 60 mg of $Fe(SO_4)_2 \cdot 7\ H_2O$ (≥99%; Sigma
619 Aldrich) and 20 mg of $Ni(SO_4)_2 \cdot 6H_2O$ (99%; Sigma Aldrich) were put in a glass bottle and 200
620 mL of 0.5 M $KHCO_3$ (pH 8.3, purged with Ar gas purged for 30 min before use) was introduced,
621 resulting in a transparent and yellow solution. For deposition, under illumination (AM 1.5G,

100 mW/cm^2), linear sweep voltammetry was conducted with a bias of −0.3 V to 0.5 V against the reference electrode (Ag/AgCl) for 12–15 times with pre-treatment of −0.3 V for 5 s. Sequential linear sweep voltammetry resulted in reduced current density and over-deposition of $NiFeO_x$. After deposition, the photoelectrode was taken out and washed with copious amounts of DI water. Right after being taken out, the photoelectrode showed a slightly darkened colour ($Ni(OH)_2$ species) but gradually changes to a colour identical to that of the photoelectrode before $NiFeO_x$ deposition. The photoelectrodes were stored in an Ar gas-filled bottle before use.

Characterisation

The surface morphology of Sb_2Se_3 thin films were analysed via Field Emission Scanning Electron Microscope (FE-SEM) (JSM-7001F, JEOL Ltd, Tokyo, Japan). The crystallinity of the samples was investigated using XRD (MiniFlex 600, Rigaku, Tokyo, Japan) with Cu Kα radiation (λ=1.54178 Å). The surface reflectance of the Sb_2Se_3 thin films was measured using a UV-vis spectrophotometer (V-670, JASCO, Easton, MD, USA). UV-Vis absorbance of $BiVO_4$ was recorded with a UV/Vis spectrometer (UV-2401PC, Shimadzu). As a reference, $BaSO_4$ powder was used. Additionally, KPFM (SPA 400, Seiko Instrument Inc., Chiba, Japan) measurements were performed using a gold-coated cantilever (SI-DF3-A).

Determination of photoelectrochemical performance

PEC measurements for Sb_2Se_3 photocathodes were performed in a typical three-electrode system with a Ag/AgCl/KCl (4M) reference electrode and a Pt wire counter electrode. The Sb_2Se_3 photocathodes were submerged in an acidic (H_2SO_4, pH ~ 1) or a neutral (phosphate buffer, pH ~ 6.25) electrolyte, and simulated solar light illumination. Calibration of the 1-sun level was performed using a standard Si reference cell certified by the Newport Corporation, consisting of a readout device and a 2 × 2 cm^2 calibrated solar cell made of monocrystalline

646 silicon. During calibration, the Si reference cell was located at the same position of the sample
647 for PEC measurement. The scan rate for the J–V curves was 5 mV s^{-1}. For Sb_2Se_3
648 photocathodes, the applied potentials were recorded against the RHE to allow comparison with
649 previously reported results, employing the relationship $E_{RHE}=E_{Ag/AgCl}+0.059\ pH+0.197$. IPCE
650 for Sb_2Se_3 photocathodes was measured with an electrochemical workstation (Zennium,
651 Zahner, Germany) combined with a potentiostat (PP211, Zahner, Germany) under
652 monochromatic light.

653 PEC performance of the $BiVO_4$ photoanode was measured with a photoanode as the
654 working electrode, Pt mesh as the counter electrode, and Ag/AgCl (3M NaCl) as the reference
655 electrode. The scan rate for the J–V curves was 20 mV s^{-1}. For electrolyte, 0.5 M potassium
656 phosphate (K_2HPO_4 or KPi) buffer + 0.01 M V_2O_5 (pH 7.0) was used as a standard electrolyte
657 as reported previously for the borate buffer (pH 9.5).[52] To accelerate dissolution of V_2O_5, it
658 was placed in oven at 80 °C for 3 h. The pH of the KPi buffer barely changed (less than 0.01)
659 while the pH of 8 or 9 showed a noticeable change that could be compensated by adding a
660 small amount of 0.5 M KOH. Potentials were recorded with correction according to the Nernst
661 relationship $E_{RHE} = E_{Ag/AgCl} + 0.0591\ pH + 0.209$, in which $E_{Ag/AgCl}$ is the applied bias potential
662 and 0.209 is a conversion factor from the Ag/AgCl electrode to the RHE scale. The
663 electrochemical data for $BiVO_4$ photoanodes were recorded by using a potentiostat (IviumStat,
664 Ivium Technologies). A 300 W Xenon lamp was used to produce simulated 1 sun light
665 irradiation conditions (AM 1.5G, 100 mW/cm^2) employing a solar simulator (Oriel 91160)
666 with an AM 1.5G filter calibrated with a reference cell certified by the National Renewable
667 Energy Laboratories, USA.

668 For the $BiVO_4$–Sb_2Se_3 tandem cell, black masked (0.32–0.36 cm^2) photoelectrodes
669 were aligned with a spacing of ~0.5 cm in a single electrolyte bed reactor. Photocurrent of
670 Sb_2Se_3 was recorded with or without the $BiVO_4$ photoelectrode (fully modified,

671 $NiFeO_x$/H,Mo:$BiVO_4$) under backward scan (~0.5 V_{RHE}–0 V_{RHE}). The $BiVO_4$ photoelectrode
672 was scanned in the forward scan (0.2 V_{RHE}–1.4 V_{RHE}). For the $BiVO_4$–Sb_2Se_3 two-electrode
673 full cell, $BiVO_4$ was set as the working electrode and Sb_2Se_3 was set as the counter electrode.
674 Bias was applied towards the counter electrode and thus 0 V against the counter electrode
675 indicated a 0 V potential applied to the full cell. For linear sweep, forward scan was applied
676 for the $BiVO_4$–Pt rod (0.3–1.3 V) or $BiVO_4$–Sb_2Se_3 (–0.3 V to 0.5 V). All scans were
677 performed with 10 s of pre-treatment at the initial potential at a speed of 20 mV/s.

678 IPCE measurements for $BiVO_4$ and Sb_2Se_3 behind $BiVO_4$ were conducted using a
679 300 W Xe lamp as the light source with a liquid IR filter and a monochromator (Oriel
680 Cornerstone 130 1/8 m monochromator) with a bandwidth limit of 5 nm. The intensity of light
681 was measured before IPCE measurements by a photodiode detector (Oriel 70260). Calculation
682 of IPCE was carried out according to the equation:

683 $$IPCE(\%) = \frac{1240 \times \mathrm{J}}{\lambda \times P} \times 100$$

684 where J = photocurrent density (mA cm^{-2}), P = light power density (mW cm^{-2}) at λ, and λ =
685 wavelength of incident light (nm). J was gathered under the condition that the PEC cell
686 individually installed and the constant potential applied for a photoelectrode and wavelength
687 of illuminated beam (1 cm × 1 cm) was periodically changed. The active area of the
688 characterised photoelectrode was preferably smaller than this beam source (0.32–0.36 cm^2).
689 The scanning wavelength range was 300–1100 nm with interval of 10 nm/7 s.

690

691 **Acknowledgements**

692 This work was supported by a National Research Foundation (NRF) of Korea grant (No.
693 2012R1A3A2026417); a Creative Materials Discovery Program (NRF-2018M3D1A1058793)

694 funded by the Ministry of Science and ICT; the Korea Center for Artificial Photosynthesis
695 (KCAP, No. 2009-0093880), funded by the MSIT; and Project No. 10050509, funded by the
696 MOTIE of Republic of Korea.

697 **Author contributions**

698 W. Yang conceived the idea, organised the collaboration, conducted experiments, analysed the
699 data, and wrote the manuscript. J. H. Kim prepared the $BiVO_4$ photoanodes, tested the tandem
700 device, and co-wrote the manuscript. O. S. Hutter and L. J. Phillips prepared and optimised the
701 Sb_2Se_3 thin films via the CSS method. J. Tan, J. Park, and H. Lee assisted in device optimisation
702 and data analysis for the Sb_2Se_3 photocathodes. J. D. Major helped to the idea and manuscript
703 preparation. J. S. Lee directed the research and contributed to the writing of the manuscript. J.
704 Moon designed and supervised the project, directed the research, and contributed to the writing
705 of the manuscript.

706 **Additional Information**

707 Supplementary information is available online. Reprints and permissions information are
708 available online at www.nature.com/reprints.

709 **Competing interests**

710 The authors declare no competing ~~financial~~ interests.

711 **Data availability**

712 The data that support the plots within this paper and other findings of this study are available
713 from the corresponding author upon reasonable request.

714

715

References

1 Cheng, W.-H. *et al.* Monolithic photoelectrochemical device for direct water splitting with 19% efficiency. *ACS Energy Lett.* **3**, 1795-1800 (2018).

2 Turner, J. A. Shining a light on solar water splitting—Response. *Science* **344**, 469-470 (2014).

3 Sivula, K. & Van De Krol, R. Semiconducting materials for photoelectrochemical energy conversion. *Nat. Rev. Mater.* **1**, 15010 (2016).

4 Kim, J. H., Hansora, D., Sharma, P., Jang, J.-W. & Lee, J. S. Toward practical solar hydrogen production–an artificial photosynthetic leaf-to-farm challenge. *Chem. Soc. Rev.* **48**, 1908-1971 (2019).

5 Yao, T., An, X., Han, H., Chen, J. Q. & Li, C. Photoelectrocatalytic materials for solar water splitting. *Adv. Energy Mater.* **8**, 1800210 (2018).

6 Hu, S., Xiang, C., Haussener, S., Berger, A. D. & Lewis, N. S. An analysis of the optimal band gaps of light absorbers in integrated tandem photoelectrochemical water-splitting systems. *Energy Environ. Sci.* **6**, 2984-2993 (2013).

7 Pinaud, B. A. *et al.* Technical and economic feasibility of centralized facilities for solar hydrogen production via photocatalysis and photoelectrochemistry. *Energy Environ. Sci.* **6**, 1983-2002, (2013).

8 Fujishima, A. & Honda, K. Electrochemical photolysis of water at a semiconductor electrode. *Nature* **238**, 37-38, (1972).

9 Tamirat, A. G., Rick, J., Dubale, A. A., Su, W.-N. & Hwang, B.-J. Using hematite for photoelectrochemical water splitting: a review of current progress and challenges. *Nanoscale Horizons* **1**, 243-267 (2016).

10 Kim, J. H. & Lee, J. S. Elaborately modified $BiVO_4$ photoanodes for solar water splitting. *Adv. Mater.* **31**, 1806938 (2019).

11 Paracchino, A., Laporte, V., Sivula, K., Grätzel, M. & Thimsen, E. Highly active oxide photocathode for photoelectrochemical water reduction. *Nat. Mater.* **10**, 456 (2011).

12 Yang, W. *et al.* Molecular chemistry-controlled hybrid ink-derived efficient Cu_2ZnSnS_4 photocathodes for photoelectrochemical water splitting. *ACS Energy Lett.* **1**, 1127-1136, (2016).

13 Yu, Y.-X. *et al.* Solution-processed Cu_2S photocathodes for photoelectrochemical water splitting. *ACS Energy Lett.* **3**, 760-766 (2018).

14 Oh, Y., Yang, W., Kim, J., Jeong, S. & Moon, J. Enhanced photocurrent of transparent $CuFeO_2$ photocathodes by self-light-harvesting architecture. *ACS Appl. Mater. Interfaces* **9**, 14078-14087 (2017).

15 Song, A. *et al.* Cu:NiO as a hole-selective back contact to improve the photoelectrochemical performance of $CuBi_2O_4$ thin film photocathodes. *J. Mater. Chem. A* **7**, 9183-9194 (2019).

16 Zhang, L. *et al.* Solution-processed $CuSbS_2$ thin film: A promising earth-abundant photocathode for efficient visible-light-driven hydrogen evolution. *Nano Energy* **28**, 135-142 (2016).

17 Huang, X. *et al.* Simple eco-friendly synthesis of the surfactant free SnS nanocrystal toward the photoelectrochemical cell application. *Scientific reports* **7**, 16531 (2017).

18 Zhou, Y. *et al.* Thin-film Sb_2Se_3 photovoltaics with oriented one-dimensional ribbons and benign grain boundaries. *Nat. Photon.* **9**, 409 (2015).

19 Wang, L. *et al.* Stable 6%-efficient Sb_2Se_3 solar cells with a ZnO buffer layer. *Nat. Energy* **2**, 17046 (2017).

20 Chen, C. *et al.* Characterization of basic physical properties of Sb_2Se_3 and its relevance for photovoltaics. *Front. Optoelectron.* **10**, 18-30 (2017).

21 Ghosh, G. The Sb-Se (antimony-selenium) system. *J. phase equilibria* **14**, 753-763 (1993).

22 Prabhakar, R. R. *et al.* Photocorrosion-resistant Sb_2Se_3 photocathodes with earth abundant MoS_x hydrogen evolution catalyst. *J. Mater. Chem. A* **5**, 23139-23145 (2017).

23 Kim, J. *et al.* Self-oriented Sb_2Se_3 nanoneedle photocathodes for water splitting obtained by a simple spin-coating method. *J. Mater. Chem. A* **5**, 2180-2187 (2017).

24 Yang, W. *et al.* Adjusting the anisotropy of 1D Sb_2Se_3 nanostructures for highly efficient photoelectrochemical water splitting. *Adv. Energy Mater.* **8**, 1702888 (2018).

25 Tan, J. *et al.* Fullerene as a photoelectron transfer promoter enabling stable TiO_2-protected Sb_2Se_3 photocathodes for photo-electrochemical water splitting. *Adv. Energy Mater.* **9**, 1900179 (2019).

26 Lee, H. *et al.* Cu-doped NiO_x as effective hole-selective layer for high-performance Sb_2Se_3 photocathode for photoelectrochemical water splitting. *ACS Energy Lett.* **4**, 995-1003 (2019).

27 Park, J. *et al.* Efficient solar to hydrogen conversion from neutral electrolytes using morphology-Controlled Sb_2Se_3 light absorber. *ACS Energy Lett.* **4**, 517-526 (2019).

28 Phillips, L. J., Savory, C. N, Hutter, O. S., Yates, P. J., Shiel, H., Mariotti, S., Bowen, L., Birkett, M., Durose, Ken., Scanlon, D. O. & Major, J. D. Current enhancement via a TiO_2 window layer for CSS Sb_2Se_3 solar cells: performance limits and high V_{oc}. *IEEE J. Photovoltaics* **9**, 544-551 (2019).

29 Major, J. D. *et al.* A low-cost non-toxic post-growth activation step for CdTe solar cells. Nature **511**, 334-337 (2014)

30 Guo, Q. *et al.* The growth of a $CH_3NH_3PbI_3$ thin film using simplified close space sublimation for efficient and large dimensional perovskite solar cells. *Energy Environ. Sci.* **9**, 1486-1494 (2016).

31 Hutter, O. S., Phillips, L. J., Durose, K. & Major, J. D. 6.6% efficient antimony selenide solar cells using grain structure control and an organic contact layer. *Solar Energy Mater. Solar Cells* **188**, 177-181 (2018).

32 Yang, W. *et al.* Time-resolved observations of photo-generated charge-carrier dynamics in Sb_2Se_3 photocathodes for photoelectrochemical water splitting. *ACS nano* **12**, 11088-11097 (2018).

33 Zhang, J. *et al.* Alternative back contacts for Sb_2Se_3 solar cells. *Solar Energy* **182**, 96-101 (2019).

34 Tilley, S. D., Schreier, M., Azevedo, J., Stefik, M. & Graetzel, M. Ruthenium oxide hydrogen evolution catalysis on composite cuprous oxide water-splitting photocathodes. *Adv. Funct. Mater.* **24**, 303-311 (2014).

35 Vijselaar, W. *et al.* Spatial decoupling of light absorption and catalytic activity of Ni–Mo-loaded high-aspect-ratio silicon microwire photocathodes. *Nat. energy* **3**, 185 (2018).

36 Kumagai, H. *et al.* Efficient solar hydrogen production from neutral electrolytes using surface-modified $Cu(In,Ga)Se_2$ photocathodes. *J. Mater. Chem. A* **3**, 8300-8307, (2015).

37 C. A. Rodriguez et al., "Design and cost considerations for practical solar-hydrogen generators", *Energy Environ. Sci.*, **7**, 3828-3835 (2014).

38 M. R. Shaner et al., "A comparative technoeconomic analysis of renewable hydrogen production using solar energy", *Energy Environ. Sci.*, **9**, 2354-2371 (2016).

39 J. Kibsgaard & I. Chorkendorff, "Considerations for the scaling-up of water splitting catalysts", *Nat. Energy.*, **4**, 430-433 (2019).

40 Chen, C. *et al.* Efficiency improvement of Sb_2Se_3 solar cells via grain boundary inversion. *ACS Energy Lett.* **3**, 2335-2341 (2018).

41 Vishwakarma, M., Varandani, D., Andres, C., Romanyuk, Y. E., Haass, S. G., Tiwari, A. N., Mehta, M. R. A direct measurement of higher photovoltage at grain boundaries in CdS/ CZTSe solar cells using KPFM technique. *Sol. Energy Mater. Sol. Cells* **183**, 43-40 (2018)

42 Kim, G. Y., Kim, J., Jo, W., Son, D.-H., Kim, D.-H., Kang, J.-K. Nanoscale investigation of surface potential distribution of $Cu_2ZnSn(S,Se)_4$ thin films grown with additional NaF layers. *Nano Convergence* **1**, 27 (2014)

43 J. Luo et al., Cu_2O Nanowire Photocathodes for Efficient and Durable Solar Water Splitting, *Nano Lett.*, **16**, 1848-1857 (2016).

44 Kemppainen, E. *et al.* Scalability and feasibility of photoelectrochemical H_2 evolution: the ultimate limit of Pt nanoparticle as an HER catalyst. *Energy Environ. Sci.* **8**, 2991-2999 (2015).

45 Chen, M. *et al.* Spatial control of cocatalysts and elimination of interfacial defects towards efficient and robust CIGS photocathodes for solar water splitting. *Energy Environ. Sci.* **11**, 2025-2034 (2018).

46 Yang, W., Prabhakar, R. R., Tan, J., Tilley, S. D., Moon, J., Strategies for enhancing the photocurrent, photovoltage, and stability of photoelectrodes for photoelectrochemical water splitting. *Chem. Soc. Rev.*, **48**, 4979 (2019).

47 Prévot, M. S. & Sivula, K. Photoelectrochemical tandem cells for solar water splitting. *J. Phy. Chem. C* **117**, 17879-17893 (2013).

48 Kobayashi, H. *et al.* Development of highly efficient $CuIn_{0.5}Ga_{0.5}Se_2$-based photocathode and application to overall solar driven water splitting. *Energy Environ Sci.* **11**, 3003-3009 (2018).

49 Laskowski, F. A., Nellist, M. R., Qiu, J. & Boettcher, S. W. Metal oxide/(oxy) hydroxide overlayers as hole collectors and oxygen-evolution catalysts on water-splitting photoanodes. *J. Am. Chem. Soc.* **141**, 1394-1405 (2018).

50 Ma, Y., Kafizas, A., Pendlebury, S. R., Le Formal, F. & Durrant, J. R. Photoinduced absorption spectroscopy of CoPi on $BiVO_4$: the function of CoPi during water oxidation. *Adv. Func. Mater.* **26**, 4951-4960 (2016).

51 Toma, F. M. *et al.* Mechanistic insights into chemical and photochemical transformations of bismuth vanadate photoanodes. *Nat. comm.* **7**, 12012 (2016).

52 Lee, D. K. & Choi, K.-S. Enhancing long-term photostability of $BiVO_4$ photoanodes for solar water splitting by tuning electrolyte composition. *Nat. Energy* **3**, 53 (2018).

53 Mayer, M. T. Photovoltage at semiconductor–electrolyte junctions. *Curr. Opinion Electrochem.* **2**, 104-110 (2017).

54 Kaneko, H., Minegishi, T., Kobayashi, H., Kuang, Y. & Domen, K. Suppression of poisoning of photocathode catalysts in photoelectrochemical cells for highly stable sunlight-driven overall water splitting. *J. Chem. Phy.* **150**, 041713 (2019).

55 Pan, L. *et al.* Boosting the performance of Cu_2O photocathodes for unassisted solar water splitting devices. *Nat. Cat.* **1**, 412 (2018).

56 Higashi, T. *et al.* Overall water splitting by photoelectrochemical cells consisting of $(ZnSe)_{0.85}(CuIn_{0.7}Ga_{0.3}Se_2)_{0.15}$ photocathodes and $BiVO_4$ photoanodes. *Chem. Comm.* **53**, 11674-11677 (2017).

57 Wick-Jaliat. Rene, et al. Stable and tunable phosphonic acid dipole layer for band edge engineering of photoelectrochemical and photovoltaic heterojunction devices. Energy Environ. Sci. **12**, 1901-1909 (2019).

58 Kim, J. H. *et al.* Wireless solar water splitting device with robust cobalt-catalyzed, dual-doped $BiVO_4$ photoanode and perovskite solar cell in Tandem: A dual absorber artificial leaf. *ACS Nano* **9**, 11820-11829 (2015).

59 Hao, Y., Deng, J., Zhou, L., Sun, X. & Zhong, J. Depth-reduction induced low onset potential of hematite photoanodes for solar water oxidation. *RSC Adv.* **5**, 31086-31090 (2015).
60 Li, F. *et al.* An iron-based thin film as a highly efficient catalyst for electrochemical water oxidation in a carbonate electrolyte. *Chem. Commun.* **52**, 5753-5756 (2016).